On-Chip Mach-Zehnder-Like Interferometer for Atomic Spin Precession Detection

Zhibo Cui, Xiangyang Zhou, Dongbi Bai, Weiyi Wang, and Zhen Chai

***Abstract*—At present, most atomic spin precession detection schemes use discrete optical elements, which lead to bulky detection systems. However, chip-based spin precession detection schemes lack modulation, resulting in lower detection sensitivity. In this paper, we propose and simulatively demonstrate an integrated atomic spin precession detection scheme using an on-chip Mach-Zehnder-like interferometer. An on-chip polarization sorter is designed, with contrast ratio of 24 dB and coupling efficiency of 16.8% at 795 nm. With this device, linearly polarized probe light that experienced optical rotation can be split and coupled into two waveguide arms of the interferometer. To avoid the effect of low frequency noise, our scheme uses a micro-heater to modulate the phase difference signal, allowing for high sensitivity detection. The whole detection system can reach micron size, which provides a practical new technique for high precision atomic sensors that can be integrated into chips.**

***Index Terms*—On-chip, polarization sorter, Mach-Zehnder-like interferometer, phase modulation, atomic spin precession detection.**

I. Introduction

SPIN is an intrinsic property of atoms, and atomic spin precession is highly sensitive to both magnetic field and inertial rotation [1], [2]. Atomic sensors based on atomic spin effect, such as atomic clocks [3], [4], atomic magnetometers [5], [6], and atomic spin gyroscopes [7], [8], have been rapidly developed in recent decades. The heart of atomic sensors is optical pumping and detection [9], [10], where optical pumping is a prerequisite for atomic state preparation and atomic spin precession detection is the key to achieving high performance measurements in atomic sensors.

Manuscript received 7 February 2023; revised 21 March 2023; accepted 22 March 2023. Date of publication 27 March 2023; date of current version 19 April 2023. This work was supported in part by Beijing Natural Science Foundation under Grant 4232071, in part by the National Natural Science Foundation of China under Grant 11804008, and in part by the Hefei National Laboratory of China under Grant 2021ZD0300500. *(Corresponding author: Zhen Chai.)*

Zhibo Cui and Weiyi Wang are with the Key Laboratory of Ultra-Weak Magnetic Field Measurement Technology, Ministry of Education, School of Instrumentation and Optoelectronic Engineering, Beihang University, Beijing 100191, China, and also with the Hangzhou Innovation Institute, Beihang University, Hangzhou 310052, China (e-mail: 17320290831@163.com; weiyi-wang@buaa.edu.cn).

Xiangyang Zhou and Zhen Chai are with the Key Laboratory of Ultra-Weak Magnetic Field Measurement Technology, Ministry of Education, School of Instrumentation and Optoelectronic Engineering, Beihang University, Beijing 100191, China, also with the Hangzhou Innovation Institute, Beihang University, Hangzhou 310052, China, and also with the Hefei National Laboratory, Hefei 230088, China (e-mail: xyzhou@buaa.edu.cn; zhenchai@buaa.edu.cn).

Dongbi Bai is with the Hangzhou Innovation Institute, Beihang University, Hangzhou 310052, China (e-mail: baidongbi@gmail.com).

Digital Object Identifier 10.1109/JPHOT.2023.3262309

At present, most detection schemes use a non-resonant, linearly polarized probe beam to detect atomic spin precession by measuring the polarization rotation angle (namely, optical rotation angle) before and after passing through a vapor cell containing the optically pumped atoms [11]. The polarization differential detection (PDD) method and the polarization modulated detection (PMD) method are two spin precession detection techniques based on linearly polarized light that have been proposed by researchers. The PDD method, which works in the DC and low frequency bands, has a simple optical structure and is effective at suppressing the common mode noise from the detected beam, but is unable to do so in the presence of low frequency noise such as 1/f noise [12], [13]. In order to suppress the low frequency noise, a number of PMD methods based on modulation techniques were introduced [14], [15]. With the addition of the modulation module, the PMD methods can achieve highly accurate detection of atomic spin precession signals under laboratory conditions. However, the modulation module itself suffers from drift issues and is susceptible to fluctuations in ambient temperature, light source power, wavelength, and magnetic field, necessitating the introduction of sophisticated means of control [16], [17]. Another atomic spin precession detection method is to detect the phase difference of circularly polarized light (CPL), such as Liu et al. used a Sagnac-like interferometer to detect the phase difference of CPL, and also used a phase modulator to modulate the phase difference signal, so as to achieve the effect of filtering out low frequency noise [18].

The urgent demand for high spatial resolution bio-magnetic imaging in the medical field [19], [20] and micro positioning navigation-timing technology (Micro-PNT) [21] in military and civilian fields has made chip integration of atomic devices become a hot topic of research in recent years. Recent rapid developments in the field of integrated photonics, especially in silicon (Si) photonics, have made it possible to integrate multi-functional conventional optics on a chip [22], [23]. Therefore, it is promising to achieve chip-based integration of atomic spin precession detection systems through emerging integrated photonics and nanofabrication techniques, which can facilitate miniaturization and mass production of atomic devices. In the last two years, PDD methods have been used to chip-based integration of atomic spin precession detection systems. For instance, Sebbag et al. developed a nanoscale photonic spin sorter (PSS) to measure the polarization of linearly detection light [24]. Hu et al. achieved the coupling and polarization splitting of detection light using an integrated polarization-splitting grating

coupler [25]. However, both the aforementioned methods are based on differential detection, which lacks modulation and is unable to mitigate the impact of low frequency 1/f noise. It is therefore urgently necessary to develop a compact system with improved stability and sensitivity for atomic spin precession detection.

In this paper, we propose and simulate an on-chip Mach-Zehnder-like interferometer for atomic spin precession detection. Based on an on-chip polarization sorter, which is composed of seven rotating Si antennas and low-loss silicon-nitride (Si_3N_4) waveguides, the interferometer enables effective polarization-splitting and coupling at the wavelength of the detection light (795 nm). Linearly polarized light carrying the optical rotation angle is separated into left circularly polarized light (LCPL) and right circularly polarized light (RCPL) by the polarization sorter, and the phase difference between the LCPL and RCPL is then detected by the interferometer to obtain the optical rotation angle. Compared with the single-fiber Sagnac-like interferometer [18], the integrated Mach-Zehnder-like interferometer based on waveguide coupling has a very small size and enables realize phase detection on a chip, which makes it possible to design a chip-based detection scheme. Additionally, the waveguide Mach-Zehnder-like interferometer allows phase modulate through thermo-optical effect. We use a micro-heater to apply a phase modulation signal to one arm of the interferometer, which effectively inhibits the influence of low frequency noise on the optical rotation angle detection and hopefully achieves higher detection sensitivity. According to Ref. [18], the system sensitivity using circularly polarized light interference method has been shown as low as 3.49 $\times$ 10^{-7}rad/Hz$^{1/2}$, which was equivalent to 3.49 fT/Hz$^{1/2}$ for the atomic magnetometer. Therefore, our scheme is expected to satisfy the requirements of miniaturized and high-precision atomic sensors detection systems. The scheme can also be made for a wide variety of magnetic sensor arrays with high spatial resolution and high magnetic field sensitivity, which is encouraging for the field of magnetic imaging.

II. Principle and Method

A. Fundamental Principles of Atomic Spin Precession Detection

At high atomic density and near zero magnetic field, it is possible to manipulate alkali metal atoms in the spin-exchange relaxation-free (SERF) state by CPL pumping, thus achieving strong nuclear-electron spin coupling and greatly improving the precision measurement and sensing ability of the atomic spin precession. As shown in Fig. 1, when the linearly polarized light passes through an alkali vapor cell in the SERF state, the optical rotation angle θ and the projection P_x^e of the atomic spin precession signal in the probe light direction (x-axis in the Fig. 1) can be expressed as [26]:

$$\theta = \frac{\pi}{3} n l r_e c P_x^e \left\{ \mathrm{Im}\left[V\left(v - v_{D2}\right)\right] - \mathrm{Im}\left[V\left(v - v_{D1}\right)\right] \right\} \quad (1)$$

Where: n is the saturation vapor density of alkali metal atoms; l is the effective propagation distance of the beam through the vapor cell; r_e is the electron radius of alkali metal atoms, and c is the speed of light in vacuum. ν_{D1} and v_{D2} are the leap frequencies of the D_1 and D_2 lines of the alkali metal atoms, respectively. $\mathrm{Im}[V(v-v_{D1})]$ and $\mathrm{Im}[V(v-v_2)]$ are the imaginary parts of the Voigt contour centered on ν_{D1} and v_{D2}, respectively. The SERF state alkali vapor cell can be equated to an optically active crystal on a macroscopic scale, and its spin properties can be described by the equivalent Faraday spin equation:

$$\theta = K_V P_x^e l \quad (2)$$

$$K_V = \frac{\pi}{3} n r_e c \left\{ \mathrm{Im}\left[V\left(v - v_{D2}\right)\right] - \mathrm{Im}\left[V\left(v - v_{D1}\right)\right] \right\} \quad (3)$$

where K_V is the equivalent spin coefficient of the vapor cell. For the set vapor cell, both K_V and l are deterministic values and θ is proportional to P_x^e. By accurately measuring the spin angle θ, an accurate measurement of the atomic spin precession can be achieved.

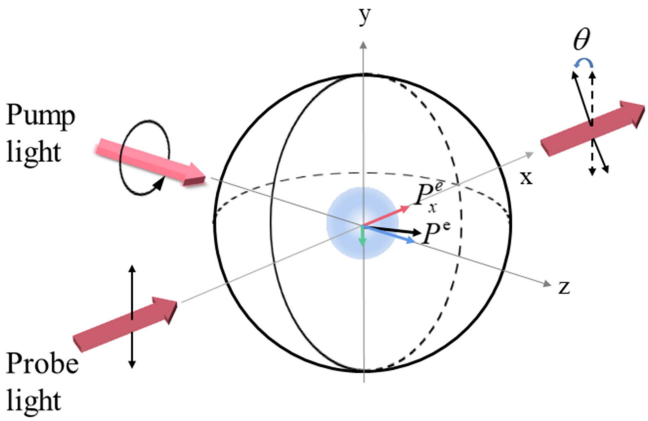

Fig. 1. SERF state atomic vapor cell and generation of the optical rotation angle θ.

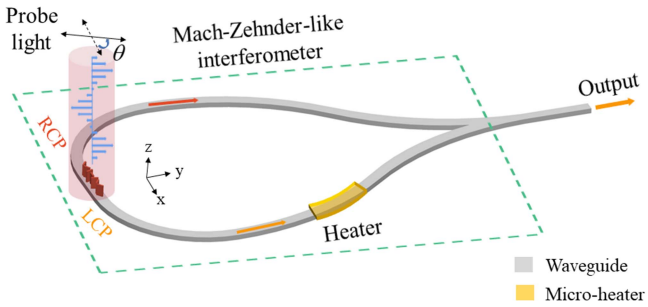

Fig. 2. Schematic of an on-chip phase-modulated spin precession detection system.

B. Principle and Design for On-Chip Phase-Modulated Spin Precession Detection System

We build the system on a CMOS-compatible photonic platform, as shown in Fig. 2, the input signal of the system is the linearly polarized detection light after passing through the alkali metal vapor cell. The dashed line indicates the polarization

direction of the linearly polarized light before passing through the vapor cell, the solid line indicates the polarization direction of the linearly polarized light after passing through the vapor cell, and θ is the angle between the two polarization directions, which is the optical rotation angle. LCPL and RCPL are formed from the linearly polarized light incident perpendicular to the polarization sorter. The two CPL components along the x-axis are then coupled into the fundamental transverse electric (TE_0) mode in two waveguide arms of the interferometer. Since the light propagating in the TE_0 mode has the same direction of vibration, interference can occur. We apply a phase modulation signal to one of the arms and measure the intensity of the output light by a miniature photodetector (PD) to calculate the magnitude of the phase difference $\Delta\varphi$. Then we obtain the θ and P_x^e according to the conversion relationship between the phase difference and the optical rotation angle $\Delta\varphi = 2\theta$ [26].

We employ a micro-heater above the waveguide to apply a phase modulation signal. The Si_3N_4 thermo-optical effect is 2.45×10^{-5}/°C [27]. As we apply voltage on the micro-heater, the temperature of the waveguide increases, which changes the refractive index of Si_3N_4 and, consequently, the accumulated phase. Considering that the heat generated by the heater will have an impact on the vapor cell, which will cover the top of the polarization sorter in the experiment, so the location of the microheater should be as far away from the polarization sorter as possible. We can consider placing the micro-heater in the rear half of the waveguide arm. Since the phase difference is weak, we test the system by modulating the phase signal and detect the output signal with a RF spectrum analyzer. We give the micro-heater a 10 kHz sinusoidal voltage signal that ranges from 0 V to 1 V. The phase difference between the two arms of the interferometer caused by the voltage signal is about 0.09 mrad. Since the phase changes with the heater power, the phase signal appears at a frequency of 20 kHz on the RF spectrum analyzer. The output light of the interferometer is detected by the miniature PD, and the optical power is then transformed into a voltage signal and examined by the RF spectrum analyzer. At this modulation frequency, the impact of 1/f noise is significantly reduced.

Assuming that the modulated phase due to the micro-heater is $\varphi_m = a \sin \omega t$, the phase difference between the two arms before interference occurs depends only on the optical rotations occurring in the cell and the differential phase modulation, and is given by:

$$\Delta\phi = \Delta\varphi + \varphi_m(t) = 2\theta + a \sin \omega t \tag{4}$$

The output light of the interferometer can be expressed as:

$$\begin{aligned} I_{out} &= I_1 + I_2 + 2\sqrt{I_1 I_2} \cos \Delta\phi \\ &= I_1 + I_2 + 2\sqrt{I_1 I_2} \left[\cos(2\theta) \cos(a \sin \omega t)\right] \\ &\quad - 2\sqrt{I_1 I_2} \left[\sin(2\theta) \sin(a \sin \omega t)\right] \end{aligned} \tag{5}$$

I_{out} contains the DC and the harmonic components of the signal, and the first harmonic component is given by the following equation:

$$I_{\text{out}} = -2K\sqrt{I_1 I_2} \sin(2\theta) J_1(a) \tag{6}$$

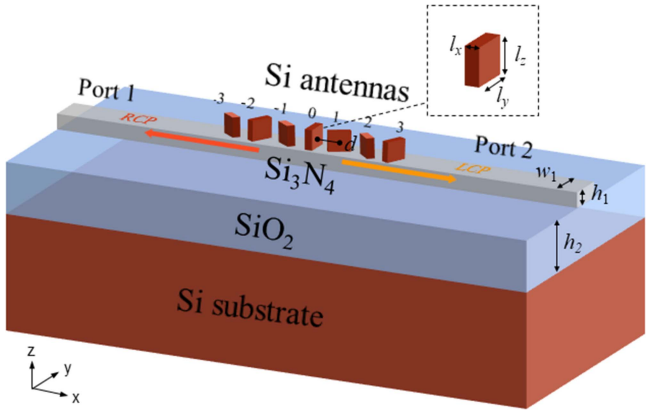

Fig. 3. Schematic diagram of the on-chip polarization sorter.

where K is the scaling factor of PD, I_1 and I_2 are the intensities of the two input beams before interference, respectively.

According to (6), I_1 and I_2 can be regarded as constants, so the first harmonic component of the interferometer output is proportional to $\sin(2\theta)$. Since the optical rotation angle θ is very small (such that $\sin\theta \approx \theta$), the output of the system can be regarded as proportional to the θ. Since the coefficient of I_{out} can be derived by calibration, the optical rotation θ and the measurement of atomic spin precession can be achieved by measuring only the optical power at the interferometer output.

III. Design and Optimization of On-Chip Polarization Sorter

We implement the design of the on-chip polarization sorter using the phase-matching condition. The three-dimensional finite difference time domain method is utilized to simulate the design process. The device is fabricated using standard Si antennas with seven Si antennas of the same shape and different orientations arranged periodically along the central axis of a 220 nm thick Si_3N_4 waveguide layer. The Si antennas with different orientations have different phase modulation of the light [28].

As shown in Fig. 3, the on-chip polarization sorter is intended to route orthogonal CPL to opposite direction. The principle of the design follows the generalized Snell's law of transmission [39], which allows the selective excitation of a specific waveguide mode after satisfying the phase-matching condition [30]:

$$\left(n_t \sin\theta_t - n_i \sin\theta_i\right) k_0 = n_{eff} k_0 = \frac{\Delta\Phi}{d} \cdot sign\left(\frac{\Delta\Phi}{d}\right) \tag{7}$$

where n_i and n_i are the refractive indices of the transmitted and incident medium [31]. θ_t and θ_i represent the refractive and incident angles. n_{eff} is the effective mode refractive index of the optical waveguide. $k_0 = 2\pi/\lambda$ represents the magnitude of the wave vector and λ is the vacuum light wavelength. $\Delta\Phi$ represents the phase difference between neighboring antennas, and d represents the antennas center-to-center interval period, so we have constant phase gradient $\Delta\Phi/d$.

For this polarization sorter, θ_i is equal to 0 and θ_t is equal to 90° in order to facilitate light propagation along the waveguide direction. When a beam of CPL is normally incident onto an anisotropic Si antenna, it is primarily scattered into waves of the opposite handedness with an interfacial phase change Φ determined by the spin direction of the CPL, and then coupled into the waveguide. This can be expressed as $\Phi = 2\sigma\beta$ [28], where $\sigma = \pm 1$ corresponds to LCPL and RCPL, β represents the rotation angle of the Si antennas. Thus the (7) can be simplified as:

$$\Delta\beta = \pm\frac{n_{eff}k_0 d}{2} \tag{8}$$

The rotation angle of the Si antennas can be determined according to (8). The height and width of the Si antennas, on the other hand, can be determined by simulation optimization. The objective function F of the optimization was defined as:

$$F = \max\left(T_L^{RCP}\right) = \max\left(T_R^{LCP}\right) \tag{9}$$

where T_L^{RCP} is the coupling efficiency of the RCPL with the TE_0 mode of the left waveguide, T_R^{LCP} is the coupling efficiency of the LCPL with the TE_0 mode of the right waveguide. The objective function F of the optimization was defined to maximize the coupling efficiency of RCPL to the TE_0 mode of the left waveguide or left circularly polarized light to the TE_0 mode of the right waveguide. In this work, we optimize the coupling to a specific waveguide mode since we are interested in the coupling efficiency of the TE_0 mode transmitted from free space to the left or right waveguide. At the optimum F, the spatial light will be maximally coupled into the waveguide TE_0 mode, which will result in a larger useful signal in the output of the system and will be beneficial for improving the signal-to-noise ratio of the system.

The width and height of the Si_3N_4 waveguide is selected as $h_1 = 220$ nm, $w_1 = 480$ nm. At this waveguide size, the mode of light propagation in the waveguide is mainly the TE_0 mode, followed by the TM_0 mode, and the higher order modes are suppressed. Coupling the light into the TE_0 mode, the effective refractive index of the waveguide in this mode is $n_{eff} = 1.58$. The period between the Si antennas is chosen to be $d = 300$ nm, which is less than half of the incident wavelength (795 nm), avoiding the non-zero level diffraction of the incident light [34]. According to (8), we have $\Delta\beta = \pm 107.32°$, and $\pm$ depend on the LCPL and RCPL. For the mth antenna, $\beta^+(m) = 107.32° \times m$ and $\beta^-(m) = -107.32° \times m$ are chosen, with m denoting the serial number of the Si antennas as $-3, -2, -1, 0, 1, 2, 3$. Next, the dimensions of the Si antennas are optimized by scanning the combination of l_x and l_y in 25 nm steps from 10 nm to 300 nm, and l_z in 25 nm steps from 10 nm to 150 nm. Then three spline interpolations are performed to maximize the objective function F. The parameters of the Si antennas on the polarization sorter are finally determined as: $l_x = 137$ nm, $l_y = 300$ nm, and $l_z = 510$ nm.

Fig. 4(a) and (b) shows the electric field intensity |E| distribution of the polarization sorter in the x-y plane under the conditions of RCPL incidence and LCPL incidence at 795 nm, respectively. It can be seen that the device exhibits excellent polarization sorting for CPL with different spin directions. Fig. 4(c) and (d) show |E| distribution and vector diagram of the right waveguide port under RCPL incidence, respectively. The contrast ratio γ is defined to quantify the directional coupling performance of the proposed sorter: $\gamma = 10\lg(T_{\text{left}}/T_{\text{right}})$,where T_{right} and T_{left} are the transmission rates of the right and left waveguide ports, respectively. Fig. 4(e) shows the coupling efficiency as a function of wavelength under RCP incidence, with contrast ratio of 24 dB and coupling efficiency of 16.8% at 795 nm. The simulation results demonstrate the excellent polarization demultiplexing functionality of the designed polarization sorter. Fig. 4(f) shows the variations of the efficiency of coupling to the TE_0 mode of the left waveguide with the size changes of the Si antennas under RCPL incidence. Where the horizontal coordinate indicates the antenna width l_x and the vertical coordinate indicates the antenna length l_y. The results show that the coupling efficiency is maintained at a high level for antennas length in the range of 120∼150 nm and antennas

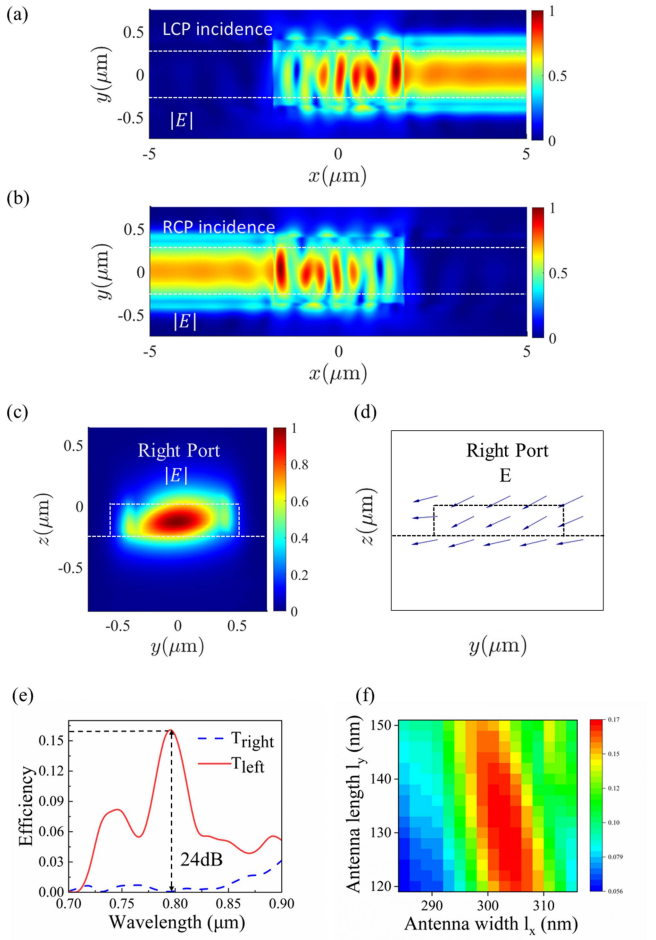

Fig. 4. |E| distribution in the x-y plane under the incidence of (a) LCPL incidence and (b) RCPL incidence. (c) |E| distribution and (d) vector diagram at the right waveguide port under RCPL incidence. (e) Coupling efficiency spectra at different wavelengths under RCPL incidence. (f) Variation of the left waveguide coupling efficiency with the size changes of the Si antennas at RCPL incidence.

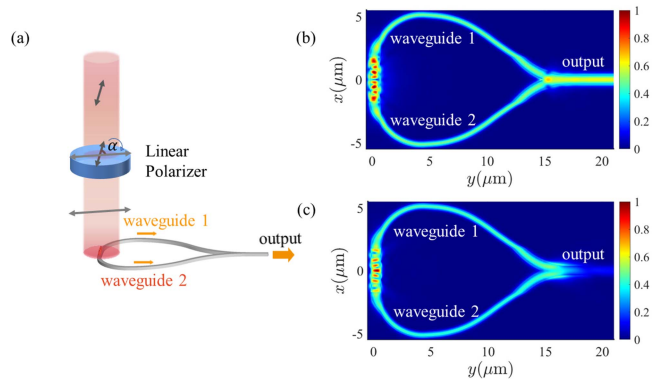

Fig. 5. (a) Schematic diagram of the setup used to test the system output at different polarization angles; (b) |E| distribution in the y-x plane for the waveguide with the x-polarized light incident; (c) |E| distribution in the y-x plane for the waveguide with the y-polarized light incident.

width in the range of 298∼308 nm. From this, the impact of fabrication error on the device performance can be analyzed.

As described above, the on-chip polarization sorter is designed to split and couple linearly polarized probe light that experienced optical rotation. Then, we constructed a Mach-Zehnder-like interferometer based on the polarization sorter for detecting phase difference signals. As shown in Fig. 2, the interferometer consists of a polarization sorter, two 90-degree curved waveguides and a Y-junction waveguide. Considering the influence of bending radius on transmission efficiency and simulation time, a 4 μm radius is selected for 90-degree curved waveguides, which achieves the optimal balance between transmission efficiency and simulation time. The Y-junction waveguide is used to meet and interfere with of two parallel-propagating light. Since the length of the straight waveguide in the sorter is 2 μm, the center-to-center distance between the two input ports of the Y-junction waveguide is 10 μm. Optimize to obtain the maximum transmission efficiency, and finally x span $L_s = 13$ μm is obtained for the s-bend sections of the Y-junction waveguide.

IV. Simulation Results and Discussion

In Section II, we theoretically analyzed the principle of on-chip spin precession detection based on the Mach-Zehnder-like interferometer. We know that the conversion accuracy of optical rotation angle and phase difference will directly affect the detection accuracy of atomic spin precession. Next, we simulate to investigate whether the conversion relationship between the rotation angle θ and phase difference $\Delta\varphi$ satisfies $\Delta\varphi = 2\theta$, and give the conditions for the practical application of the system based on the simulation results.

Assuming that the polarization direction of linearly polarized light is α to the x-axis. By rotating the linearly polarizer, the output response of the system under different α can be obtained, as shown in Fig. 5(a). When the incident light was x-polarized, the |E| distribution in the interferometer is shown in Fig. 5(b). Obviously, the light in the output waveguide shows interference enhancement, showing periodic variations in the field strength depending on the waveguide position. Therefore, when $\alpha = 0$, the two beams transmitted in waveguide 1 and waveguide 2 have the same phase. Fig. 5(c) shows the |E| distribution in the interferometer when the incident light was y-polarized, as well as the appearance of the interference elimination. It can be concluded that the two beams transmitted in waveguide 1 and waveguide 2 have the same light intensity and a phase difference of π.

As α varies from 0 to 360°, the TE_0 mode transmission efficiency of the interferometer output is measured, denoted as T. Fig. 6(a) depicts the variation of the transmission efficiency of the interferometer output with respect to the polarization angle, which shows a typical $\sin(2\alpha)$ dependency. We obtain the phase difference $\Delta\varphi$ from the reverse calculation of the interferometer output optical power and compare it with the polarization angle α, then we accurately derive the conversion relation between the polarization angle α and the phase difference $\Delta\varphi$. In order to obtain the transmission efficiency in the two waveguides before the interference, we disconnected waveguide 1 and kept only waveguide 2 for the same operation on the basis of Fig. 5(a) to obtain the TE_0 mode transmission efficiency, noted as T_1. Then we disconnected waveguide 2 and kept only waveguide 1 to obtain the TE_0 mode transmission efficiency, noted as T_2. The results are shown in Fig. 6(b). It is evident that, following beam splitting by the polarization sorter, the intensity of the light coupled to each of the two waveguide differs and depends on the polarization angle. This is caused by the structure of the polarization sorter, which is symmetric about the x-axis. A change in the polarization angle α of linearly polarized light will result in a change in coupling efficiency, and the intensity of the light in the two waveguides will exhibit alternating fluctuations. A polarization sorter with symmetry about the center can be designed in the future to address this issue.

The phase difference between the two beams of light can be found using the principle of interference of light as:

$$\begin{aligned}\Delta\varphi &= \cos^{-1}\left(\frac{I - I_1 - I_2}{2\sqrt{I_1 I_2}}\right) \\ &= \cos^{-1}\left(\frac{T - T_1 - T_2}{2\sqrt{T_1 T_2}}\right)\end{aligned} \tag{10}$$

Where I, I_1, I_2 represent the interference light intensity, the light intensity in waveguide 1 and the light intensity in waveguide 2, respectively.

The phase difference $\Delta\varphi$ can be calculated based on (10), and we chose a range of 60∼100° for the study, as shown in Fig. 7(a). It can be seen that there is an approximate relationship between half of the phase difference $\Delta\varphi/2$ and the polarization angle α, which is equal under some values of α. We rescanned the α range of 68∼68.2°, as shown in Fig. 7(b). It can be seen that there is a good agreement between $\Delta\varphi/2$ and α in this angular range. As a result, the polarization sorter performs well in some angular ranges despite its limitations in terms of coupling effectiveness to linearly polarized light.

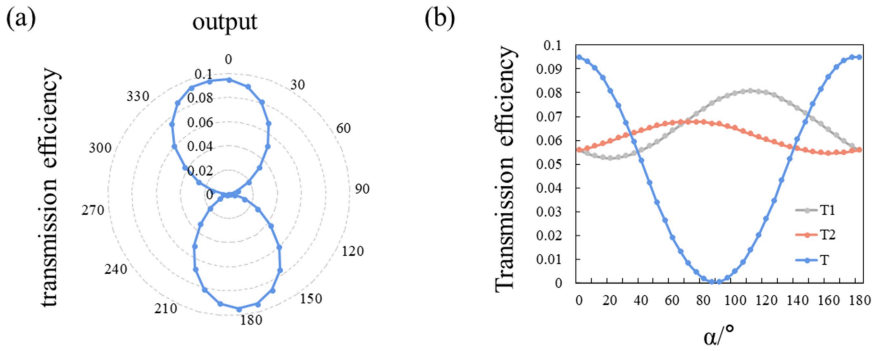

Fig. 6. (a) The relationship between the intensity of the measured output interferometric light and the polarization angle of the linearly polarized light; (b) The total transmission efficiency at the output versus when only the upper and lower waveguides are present.

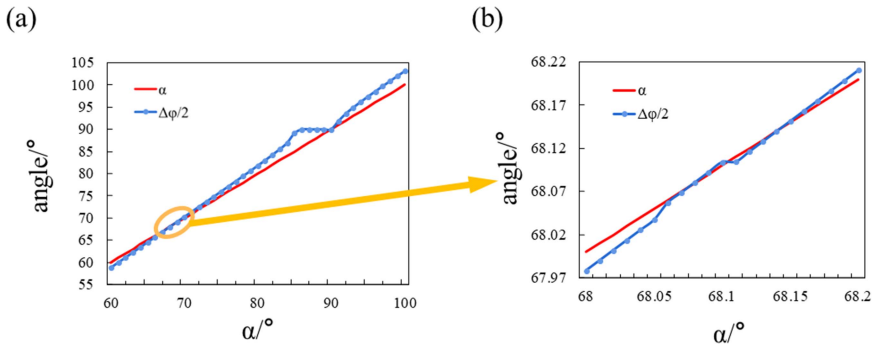

Fig. 7. (a) Relationship between the phase difference $\Delta\varphi/2$ and the polarization angle α; (b) Results after rescanning in the range of 68∼68.2°.

For miniaturized atomic sensors, such as chip-based magnetometers, the sensitivity and measurement range of 10^{-6} rad/Hz$^{1/2}$ and $10^{-7}\sim10^{-5}$ rad were expected [32]. The measurement range of the system is larger than 0.0035 rad, which is bigger than the optical rotation range for chip-based magnetometers. In practice, the initial polarization direction of the detected light can be considered to be set on 68.1°, then the phase modulation is carried out near this point, and the amplitude of the modulation is 0.003 rad, which is still within the measurement range and satisfy the requirements of both measurement range and sensitivity.

Our research uses on-chip Mach-Zehnder-like interferometer to implement the detection of atomic spin precession. The integration of the entire detection system into a photonic chip with an alkali metal vapor cell enables a highly flexible matching, allowing for the design of magnetic sensor arrays with high spatial resolution and high magnetic field sensitivity over a wide range, serving as a positive example for magnetic imaging techniques. Fig. 8 depicts the conceptual diagram of the suggested two-dimensional magnetometer array, where each on-chip Mach-Zehnder-like interferometer represents a single pixel for determining the strength of the magnetic field. The density of the interferometer and the volume of the Rb vapor cell integrated above it determine the spatial resolution, which allows the array to measure the magnitude of the magnetic field intensity in two dimensions.

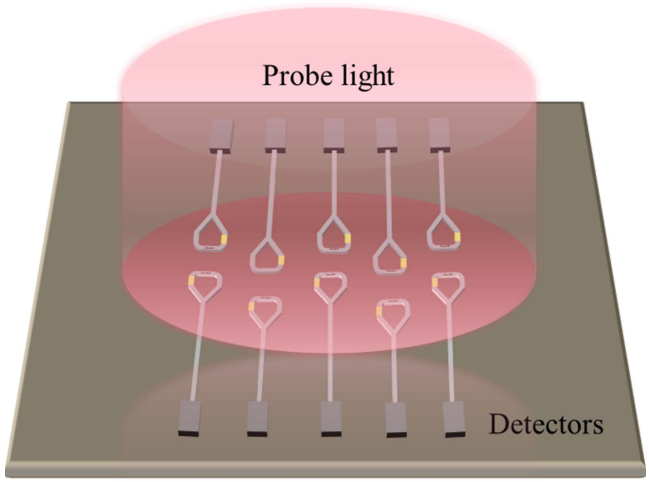

Fig. 8. Schematic diagram of 2D magnetic sensing array.

V. Conclusion

In this paper, we propose and simulate an on-chip Mach-Zehnder-like interferometer-based atomic spin precession detection scheme. For this, an on-chip polarization sorter is created. With coupling efficiency of 16.8% and contrast ratio of

24 dB, the designed on-chip polarization sorter enables effective polarization-splitting and coupling at the detection light wavelength (795 nm). Our method, which adds modulation compared to the PDD methods, uses a micro-heater to apply a phase modulation signal to one arm of the interferometer. This effectively reduces the impact of low frequency noise on the spin angle detection and is anticipated to increase detection sensitivity.

The main advantage of our atomic spin precession detection system is the union of metasurface and on-chip waveguide technology, which enables on-chip integration of the detection system with micron-level spatial resolution and high interferometric measurement sensitivity. The simulation results show that the phase difference measurement of CPL for atomic spin precession detection is a workable solution, offering a new method for high-precision, on-chip integrable atomic sensors.

REFERENCES

[1] M. J. A. De Voigt, J. Dudek, and Z. Szymański, "High-spin phenomena in atomic nuclei," *Rev. Modern Phys.*, vol. 55, no. 4, 1983, Art. no. 949.

[2] C. F. Hirjibehedin et al., "Large magnetic anisotropy of a single atomic spin embedded in a surface molecular network," *Science*, vol. 317, no. 5842, pp. 1199–1203, 2007.

[3] A. D. Ludlow et al., "Optical atomic clocks," *Rev. Modern Phys.*, vol. 87, no. 2, 2015, Art. no. 637.

[4] T. E. Mehlstäubler et al., "Atomic clocks for geodesy," *Rep. Prog. Phys.*, vol. 81, no. 6, 2018, Art. no. 064401.

[5] J. Allred et al., "High-sensitivity atomic magnetometer unaffected by spin-exchange relaxation," *Phys. Rev. Lett.*, vol. 89, no. 13, 2002, Art. no. 130801.

[6] I. K. Kominis et al., "A subfemtotesla multichannel atomic magnetometer," *Nature*, vol. 422, no. 6932, pp. 596–599, 2003.

[7] T. W. Kornack, R. K. Ghosh, and M. V. Romalis, "Nuclear spin gyroscope based on an atomic comagnetometer," *Phys. Rev. Lett.*, vol. 95, no. 23, 2005, Art. no. 230801.

[8] M. E. Limes, D. Sheng, and M. V. Romalis, "$He^3 - Xe^{129}$ comagnetometery using Rb 87 detection and decoupling," *Phys. Rev. Lett.*, vol. 120, no. 3, 2018, Art. no. 033401.

[9] W. Happer, "Optical pumping," *Rev. Modern Phys.*, vol. 44, no. 2, 1972, Art. no. 169.

[10] H. Sanada et al., "Optical pump-probe measurements of local nuclear spin coherence in semiconductor quantum wells," *Phys. Rev. Lett.*, vol. 96, no. 6, 2006, Art. no. 067602.

[11] W. Happer and B. S. Mathur, "Off-resonant light as a probe of optically pumped alkali vapors," *Phys. Rev. Lett.*, vol. 18, no. 15, 1967, Art. no. 577.

[12] D. Sheng et al., "Subfemtotesla scalar atomic magnetometry using multipass cells," *Phys. Rev. Lett.*, vol. 110, no. 16, 2013, Art. no. 160802.

[13] C. Johnson, P. D. Schwindt, and M. Weisend, "Magnetoencephalography with a two-color pump-probe, fiber-coupled atomic magnetometer," *Appl. Phys. Lett.*, vol. 97, no. 24, 2010, Art. no. 243703.

[14] G. Vasilakis et al., "Limits on new long range nuclear spin-dependent forces set with a $K- He^3$ comagnetometer," *Phys. Rev. Lett.*, vol. 103, no. 26, 2009, Art. no. 261801.

[15] Y. Hu et al., "An atomic spin precession detection method based on electro-optic modulation in an all-optical K–Rb hybrid atomic magnetometer," *J. Phys. D: Appl. Phys.*, vol. 50, no. 26, 2017, Art. no. 265001.

[16] W. Quan, Q. Wang, and Y. Zhai, "A dual closed-loop drive and control system of photoelastic modulator for atomic magnetometer," *Meas. Sci. Technol.*, vol. 29, no. 6, 2018, Art. no. 065105.

[17] Y. Hu et al., "Reduction of far off-resonance laser frequency drifts based on the second harmonic of electro-optic modulator detection in the optically pumped magnetometer," *Appl. Opt.*, vol. 56, no. 21, pp. 5927–5932, 2017.

[18] X. Liu et al., "Single-fiber Sagnac-like interferometer for optical rotation measurement in atomic spin precession detection," *J. Lightw. Technol.*, vol. 37, no. 4, pp. 1317–1324, Feb. 2019.

[19] O. Alem et al., "Magnetic field imaging with microfabricated optically-pumped magnetometers," *Opt. Exp.*, vol. 25, no. 7, pp. 7849–7858, 2017.

[20] G. Zhang et al., "Multi-channel spin exchange relaxation free magnetometer towards two-dimensional vector magnetoencephalography," *Opt. Exp.*, vol. 27, no. 2, pp. 597–607, 2019.

[21] R. Lutwak, "Micro-technology for positioning, navigation, and timing towards PNT everywhere and always," in *Proc. Int. Symp. Inertial Sensors Syst.*, 2014, pp. 1–4.

[22] W. Wang, Y. Xu, and Z. Chai, "On-chip light–atom interactions: Physics and applications," *Adv. Photon. Res.*, vol. 3, no. 12, 2022, Art. no. 2200153.

[23] L. Stern et al., "Chip-scale atomic diffractive optical elements," *Nature Commun.*, vol. 10, no. 1, pp. 1–7, 2019.

[24] Y. Sebbag et al., "Demonstration of an integrated nanophotonic chip-scale alkali vapor magnetometer using inverse design," *Light: Sci. Appl.*, vol. 10, no. 1, 2021, Art. no. 54.

[25] J. Hu et al., "Integrated polarization-splitting grating coupler for chip-scale atomic magnetometer," *Biosensors*, vol. 12, no. 7, 2022, Art. no. 529.

[26] S. J. Seltzer, "Developments in alkali-metal atomic magnetometry," Ph.D. dissertation, Dept. Phys., Princeton Univ., Princeton, NJ, USA, 2008.

[27] A. Arbabi and L. L. Goddard, "Measurements of the refractive indices and thermo-optic coefficients of Si_3N_4 and SiOx using microring resonances," *Opt. Lett.*, vol. 38, no. 19, pp. 3878–3881, 2013.

[28] Y. Guo et al., "Chip-integrated geometric metasurface as a novel platform for directional coupling and polarization sorting by spin–orbit interaction," *IEEE J. Sel. Topics Quantum Electron.*, vol. 24, no. 6, Nov./Dec. 2018, Art. no. 4700107.

[29] N. Yu et al., "Light propagation with phase discontinuities: Generalized laws of reflection and refraction," *Science*, vol. 334, no. 6054, pp. 333–337, 2011.

[30] Z. Li et al., "Controlling propagation and coupling of waveguide modes using phase-gradient metasurfaces," *Nature Nanotechnol.*, vol. 12, no. 7, pp. 675–683, 2017.

[31] Y. Meng et al., "Versatile on-chip light coupling and (de) multiplexing from arbitrary polarizations to controlled waveguide modes using an integrated dielectric metasurface," *Photon. Res.*, vol. 8, no. 4, pp. 564–576, 2020.

[32] N. Yu et al., "Light propagation with phase discontinuities: Generalized laws of reflection and refraction," *Science*, vol. 334, no. 6054, pp. 333–337, 2011.